ACCSCIENCE PUBLISHING

Journal of Seismic Exploration

ARTICLE

Application of the spatial autocorrelation method incorporating damping optimization for identifying goafs in cultural heritage sites

Jiale Liu[1], Xiaodong Wang[1]*, Yanhai Liu[2], Ke Ren[3], and Shangqing Zhang[4]

[1]Department of Geophysics and Information, College of Geoscience and Surveying Engineering, China University of Mining and Technology-Beijing, Beijing, China

[2]China Energy Shendong Coal Group Co., Ltd., Ordos, Nei Mongol Autonomous Region, China

[3]School of Remote Sensing Science and Technology, Aerospace Information Technology University, Jinan, Shandong, China

[4]Shanxi Key Laboratory of Metallogeny and Assessment of Strategic Mineral Resources, Taiyuan, Shanxi, China

Abstract

As a World Cultural Heritage Site, the Yungang Grottoes face the risk of geological disasters caused by underground goafs. To accurately detect the surrounding void zones of the grottoes and analyze their distribution and structural characteristics, this study uniquely applied the passive-source surface wave spatial autocorrelation (SPAC) method. Four high-density linear arrays were deployed in the Yungang Grottoes area to collect microtremor signals. By extracting the Rayleigh wave dispersion curve and combining it with a non-linear least-squares inversion technique incorporating a damping regularization term, a shallow shear wave velocity profile was established, successfully identifying potential low-velocity anomalies. During the inversion process, the optimized damping factor effectively suppressed the oscillation effects under complex geological conditions, significantly improving the stability and accuracy of the imaging. The results showed that 15 typical low-velocity anomalies with wave velocities below 1,200 m/s were identified, and these anomalies were highly consistent with the locations of goaf areas in historical mining data. The imaging results revealed that the goaf exhibits multiple layers and a multi-center distribution, with the L1 and L4 survey lines being the main areas of goaf activity. With a horizontal resolution of 10–20 m and a maximum detection depth of 320 m, the method presented differences in the integrity and fragmentation of underground rock masses. The SPAC method demonstrated advantages such as high resolution, non-destructive testing capability, and imaging stability in the detection of abandoned mine areas within cultural heritage sites. By optimizing the inversion regularization parameters, this study significantly improves imaging accuracy in complex geological environments, providing effective technical support for the stability assessment of the Yungang Grottoes and for the prevention and control of geological disaster risks at cultural heritage sites.

Keywords: Spatial autocorrelation method; Damping factor; Yungang Grottoes; Goaf

***Corresponding author:**
Xiaodong Wang
(bqt2300202017@student.cumtb.edu.cn)

Citation: Liu J, Wang X, Liu Y, Ren K, Zhang S. Application of the spatial autocorrelation method incorporating damping optimization for identifying goafs in cultural heritage sites. *J Seismic Explor*. 2025;34(5):18-35.
doi: 10.36922/JSE025330059

Received: August 16, 2025

Revised: October 16, 2025

Accepted: October 21, 2025

Published online: November 10, 2025

1. Introduction

As a large Buddhist cave complex built in the fifth century, the Yungang Grottoes are among the first sites to be included in the United Nations Educational, Scientific, and Cultural Organization (UNESCO) World Heritage List and are of outstanding historical, cultural, and artistic value. In recent years, due to the long-term mining of surrounding coal resources, the underground geological environment of the site has undergone significant changes.[1] In particular, the existence of goafs has become a major source of geological hazards, threatening the structural safety and long-term stability of the grottoes.[2] Accurate detection of the distribution range and structural characteristics of goafs is a key technical step in the effective protection of cultural relic sites and in the prevention and control of geological disaster risks.[3-6]

Globally, cultural heritage sites face increasingly severe threats from mining-induced geological hazards. The Wieliczka Salt Mine in Poland, a UNESCO World Heritage Site, has experienced terrain deformation due to centuries of salt extraction, with interferometric synthetic aperture radar (InSAR) technology employed for continuous monitoring.[7] In China, microtremor survey methods have been successfully applied to map collapsed columns and goafs in coal mining areas.[8,9] Despite these advances, achieving high-resolution subsurface imaging under complex geological conditions while maintaining non-invasive protocols remains challenging, particularly for heritage sites with strict construction constraints.

Various geophysical techniques have been developed for goaf detection. Martínez-Moreno *et al.*[10] used a combination of microgravity, two-dimensional (2D) electrical resistivity imaging (ERT), and induced polarization to reveal cavity structures in Spain's Algaidilla Cave. Metwaly and AlFouzan[11] applied 2D ERT for shallow goaf imaging in Saudi Arabia. Styles *et al.*[12] evaluated the applicability of microgravity in karst and abandoned mine detection. In cultural heritage contexts, passive-source methods offer particular advantages due to their non-invasive nature, strong anti-interference capability, and flexible deployment.[13-15] Zeid *et al.*[16] successfully applied the horizontal to vertical spectral ratio technology to identify ancient soil layer interfaces at Italy's Pilastri site, while Schwellenbach *et al.*[17] used passive surface waves at Sicily's Selinunte Archaeological Park to obtain high-resolution shallow velocity structures. However, inversion instability and velocity oscillations under abrupt gradient changes remain unresolved, limiting imaging quality and geological interpretation accuracy in complex scenarios.

To address these challenges, this paper introduces the spatial autocorrelation (SPAC) passive surface wave method for high-resolution goaf imaging in the Yungang Grottoes Protection Area. By extracting Rayleigh wave dispersion curves from continuous microtremor data acquired through multiple observation lines and employing multi-parameter inversion with damped regularization control, we establish shear wave velocity profiles to identify low-velocity anomaly zones indicative of goaf distributions. The adjustable damping factor suppresses non-geological oscillations caused by abrupt velocity changes, significantly improving imaging stability and geological interpretation reliability for complex structures. The research results not only fill the gap in knowledge about the near-surface structure of the region but also provide a scientific basis for assessing the potential impact of goafs on the stability of the Yungang Grottoes, offering technical support for long-term cultural heritage protection and geological disaster risk mitigation.

2. Overview of the study area

2.1. Geological overview

The study area is located in the western part of Datong city, Shanxi province, on the western edge of the Datong–Lingqiu block of the North China Platform, as shown in Figure 1. The regional structure forms part of the Shanxi Graben Basin, with Cenozoic tectonic movements as the main controlling factor.[18] The stratigraphic sequence is relatively well-developed, consisting primarily of the Archean metamorphic rock series, Triassic red beds, Jurassic coal-bearing strata, and Quaternary loose deposits from bottom to top.[19] Among them, the Jurassic Datong Formation has a thick stratum and stable rock composition, making it the main coal-bearing stratum in this area, as demonstrated in Figure 2.

The coal-bearing strata in the study area are developed from bottom to top in multiple coal-bearing layers, with interlayers of mudstone, siltstone, and fine sandstone between the coal layers, exhibiting good stratified characteristics. In terms of structure, the overall formation is monoclinal, with the strata gently dipping toward the west at an angle of approximately 8–12°. No large-scale fold structures have been observed in the region.[20] Fractures are not well developed overall; however, due to the long-term impact of mining activities, joints and fractures in the shallow rock layers are relatively well developed. Localized areas of roof collapse and mining-induced fracture zones may pose potential threats to the overall stability of the rock mass.[21]

2.2. Coal seam distribution and current mining status

The exploitable coal seams in the study area mainly include coal seams #2, #3, #7, #8, #9, #11, and #12, all of which

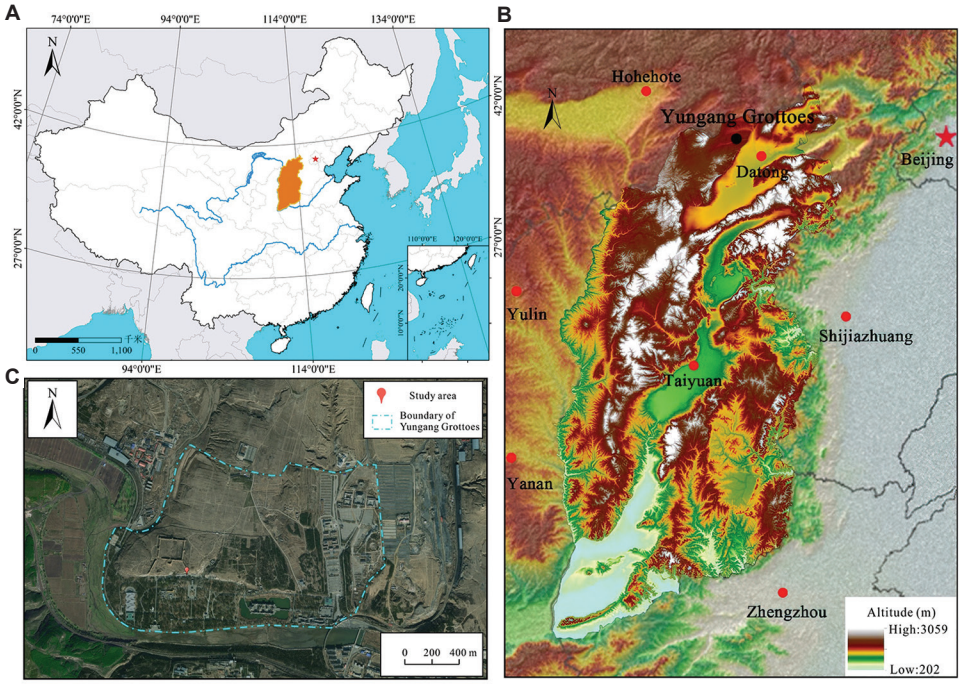

Figure 1. Research area map. (A) Shanxi province is located in North China. (B) The Yungang Grottoes are located in the northern part of Shanxi province at an average elevation of 1,186 m. (C) Yungang Grottoes study area.

occur within the Jurassic Datong coal-bearing strata.[22] There are variations in both thickness and depth among the coal seams. Seams #7, #9, and #11 are relatively stable and thick, serving as the main mining seams, as shown in Table 1. The thickness of coal seam #7 is approximately 2.36 m, buried at a depth of about 115 m. It is continuously deposited and of excellent quality, and large-scale mining has been completed. The thickness of coal seam #9 is 0.75 m, buried at a depth of approximately 125 m, and it has been the principal mining seam both currently and historically. The thickness of coal seam #11 is 1.57 m, buried at a depth of about 130 m. It is locally developed, and mining in some areas has been suspended. Other coal seams vary in thickness between 0.3 and 2.65 m, most of which are locally mineable. Due to long-term underground mining activities, numerous goafs have formed in the area. Some goafs exhibit collapse zones and fissure-type water-conducting zones at the top, while others contain significant water accumulation, posing considerable geological safety risks.

2.3. Geophysical characteristics

The surrounding rock medium in the study area mainly consists of mudstone, siltstone, and sandstone. Among these, sandstone typically has a higher wave velocity, with dense sandstone reaching wave velocities of over 1,200 m/s. Mudstone has a lower wave velocity, typically ranging from 750 to 950 m/s. Due to rock fragmentation, gas accumulation, or water accumulation, the wave velocity in goafs is significantly lower than that of the surrounding rock.[23,24] The specific wave velocity depends on the degree of fragmentation and the extent of water accumulation in the goaf.[25]

Electrical parameters also show significant differences. Normal surrounding rock has high resistivity, with siltstone and sandstone resistivities mostly ranging from 100 to 300 Ω·m, while mudstone resistivity is relatively low, approximately 50 to 150 Ω·m. In areas of water accumulation within goafs, the resistivity decreases markedly, usually to below 50 Ω·m, and locally to below 20 Ω·m. Such low-resistivity anomaly zones show strong spatial correlation with known water-filled goafs. The physical parameters of the Jurassic coal strata are shown in Table 2.

3. Research methods

3.1. Principle of passive-source surface wave exploration

SPAC is a passive surface wave detection technique based on microtremor observations. It is mainly used to extract Rayleigh wave dispersion curves and to invert underground shear wave velocity structures.[26]

The SPAC method is based on two assumptions: (i) micro-movements conform to a stationary

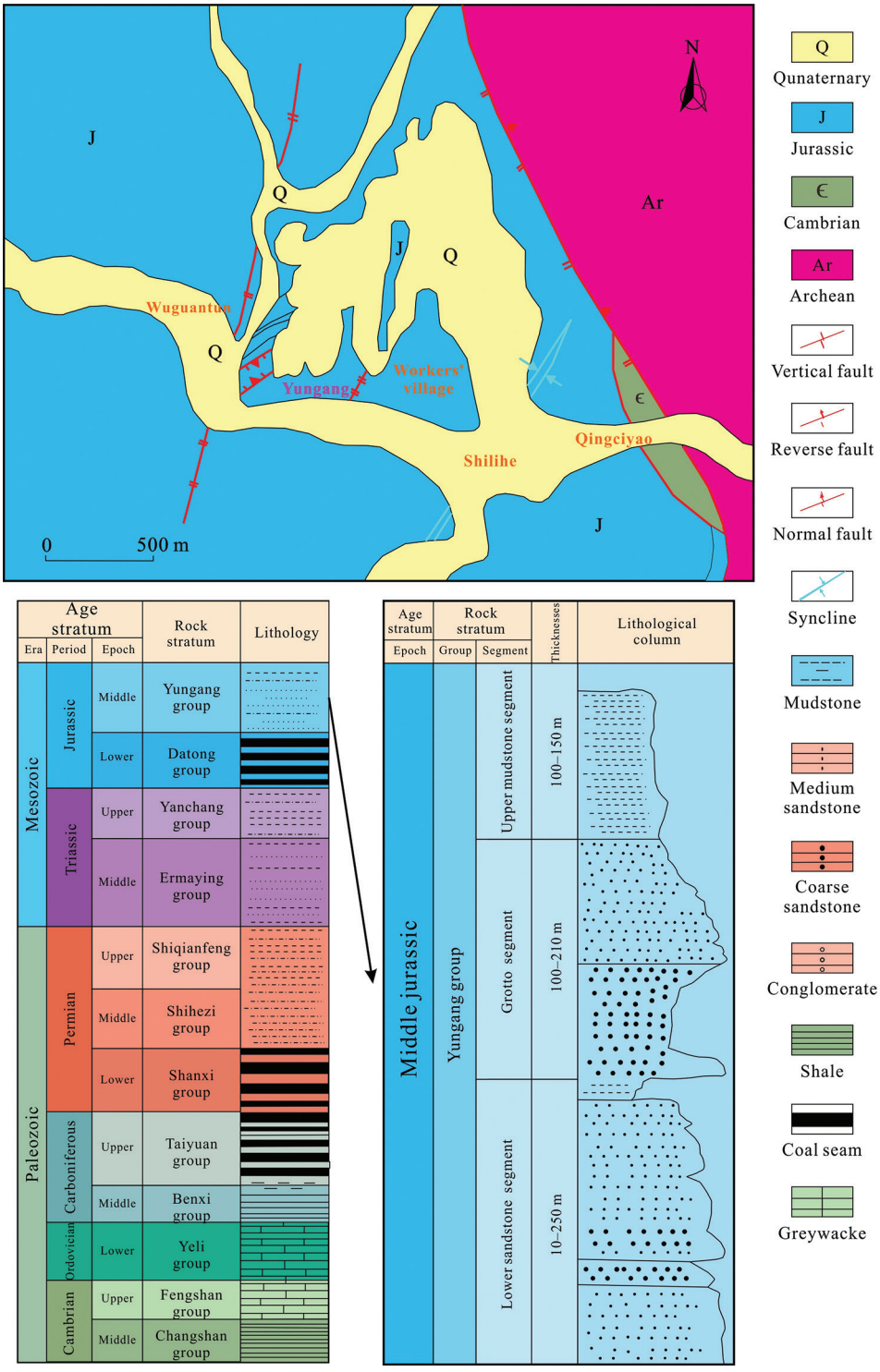

Figure 2. Geological map of Yungang Grottoes

random process in space and time, and (ii) among the various components contained in micro-movements, fundamental surface waves dominate. Let there be a reference observation point at the center point O(0,0), with a circle of observation points $A_1(r,\theta)$ distributed at a distance r around it, as shown in Figure 3. Then, the SPAC coefficient $\rho(\omega,r)$ between these two points can be expressed as **Equation (I)**:

Table 1. Characteristics of coal seams in the study area

Coal seam number	Coal seam minimum-maximum (average)/(m)	Top plate rock type	Base plate rock type
2^{-3}	1.45–6.12 (4.59)	Coarse sandstone; fine sandstone	Siltstone
3	0.10–8.82 (1.74)	Fine sandstone; siltstone	Siltstone
7^{-1}	0.00–5.50 (0.86)	Fine sandstone;	Carbonaceous mudstone
7^{-3}	0.27–4.79 (1.50)	Siltstone; fine sandstone	Sandy mudstone; Siltstone
8	0.00–3.00 (0.64)	Siltstone; fine sandstone	Siltstone; fine-grained sandstone
9	0.00–2.35 (0.75)	Fine sandstone; Sandstone	Sandy mudstone; Siltstone
11^{-1}	0.00–9.22 (1.27)	Fine sandstone; sandy mudstone	Siltstone; fine sandstone
11^{-3}	0.00–2.45 (0.30)	Sandy mudstone; siltstone	Sandy mudstone; fine sandstone
12^{-2}	0.00–9.22 (2.65)	Coarse sandstone; medium sandstone	Carbonaceous mudstone; sandy mudstone; siltstone
14^{-2}	0.00–4.67 (0.57)	Fine sandstone	Siltstone; fine sandstone; sandy mudstone

Table 2. Physical parameters of Jurassic coal strata

Rock type	Apparent density (g/cm³)	Apparent resistivity (Ω·m)	Sound time difference (μs/m)	Wave velocity (m/s)
Coal seam	1.4–1.7 (1.6)	280–930 (640)	440–640 (542)	1,563–2,273 (1,845)
Mudstone	2.1–2.4 (2.3)	54–105 (80)	291–414 (351)	2,415–3,436 (2,849)
Sandy mudstone	2.2–2.6 (2.4)	69–121 (95)	280–400 (339)	2,500–3,571 (2,950)
Siltstone	2.3–2.7 (2.5)	72–130 (103)	241–350 (301)	2,857–4,149 (3,322)
Fine sandstone	2.4–2.7 (2.6)	85–151 (115)	211–312 (262)	3,205–4,739 (3,817)
Medium sandstone	2.5–2.8 (2.7)	108–390 (250)	172–243 (212)	4,115–5,814 (4,717)
Coarse sandstone	2.6–2.8 (2.7)	138–442 (297)	124–186 (161)	5,376–8,065 (6,211)
Gravel; rock	2.7–2.8 (2.7)	145–470 (308)	114–171 (145)	5,848–8,772 (6,897)

Note: Values in parentheses represent the average.

$$\rho(\omega,r)=\frac{1}{2\pi}\int_0^{2\pi}\varphi_\omega(r,\theta)\mathrm{d}\theta \quad \text{(I)}$$

Among these, $\varphi_\omega(r,\theta)$ represents the coherence function at frequency ω, which can be expressed as **Equation (II)**:

$$\varphi_\omega(r,\theta)=\frac{u(O(0,0),t)\cdot u(A_1(r,\theta),t)}{|u(O(0,0),t)|\cdot|u(A_1(r,\theta),t)|} \quad \text{(II)}$$

Here, $u(O(0,0),t)$ and $u(A_1(r,\theta),t)$ denote the microtremor signals at the center point and surrounding observation points at time t, respectively. Under isotropic conditions, the coherence of surface waves can be expressed using the zero-order Bessel function J_0 (**Equation [III]**):

$$\rho(\omega,r)=J_0\left(\frac{\omega r}{c(\omega)}\right) \quad \text{(III)}$$

In this equation, J_0 is the zero-order Bessel function of the first kind, ω is the angular frequency, r is the distance between observation points, and $c(\omega)$ is the phase velocity at frequency ω.

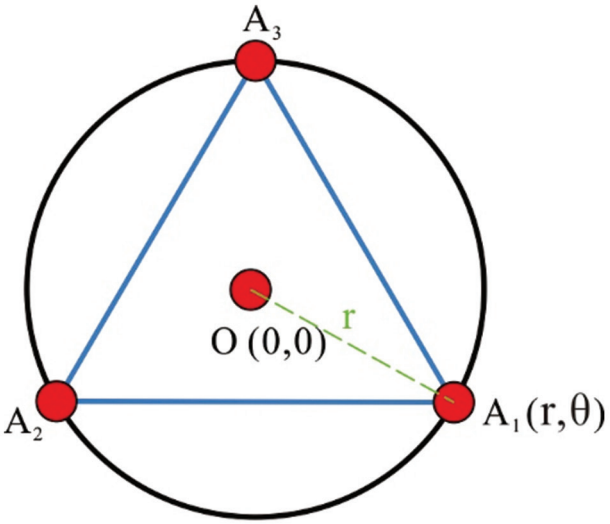

Figure 3. Single-circle observation array for the spatial autocorrelation method

By measuring the SPAC coefficient $\rho(\omega,r)$ at different distances r, the relationship between $\rho(\omega,r)$ and the Bessel function can be fitted, thereby deriving the phase velocity

$c(\omega)$ at different frequencies.[27] The curves showing the variation of these phase velocities with frequency are the surface-wave dispersion curves.[28]

The SPAC method is characterized by flexible deployment, high non-destructiveness, strong anti-interference ability, and adaptability to complex geological environments. It is particularly suitable for cultural heritage protection areas, as it does not rely on strong seismic sources and causes no disturbance to the ground surface. Therefore, it was employed in this study to detect the underground goaf in the Yungang Grottoes.

3.2. Shear wave velocity inversion

To invert the underground shear wave velocity structure from the dispersion curve, this study used a non-linear least-squares inversion algorithm and introduced a damping factor as a regularization term in the objective function to improve the stability of the inversion process and the physical plausibility of the model results.[29-31] The inversion objective function is expressed as follows (**Equation [IV]**):

$$\min_{m} \Phi(m) = \left\| d_{obs} - d_{cal}(m) \right\|^2 + \lambda^2 \left\| L(m - m_0) \right\|^2 \quad \text{(IV)}$$

Among these, m is the stratigraphic model parameter to be inverted (mainly shear wave velocity), d_{obs} and $d_{cal}(m)$ represent the measured and model-predicted dispersion data, respectively; λ is the damping factor; L is the regularization matrix; and m_0 is the prior model.

The damping factor λ in **Equation (V)** controls the trade-off between minimizing the data misfit and maintaining model smoothness. To systematically determine the optimal λ, the L-curve criterion[32] was employed, which constructs a curve by plotting $\log(\|d_{obs}\text{-}d_{cal}(m)\|)$ versus $\log(\|L(m\text{-}m_0)\|)$ for a series of candidate damping values. The optimal λ_{opt} corresponds to the corner of this L-shaped curve, where the curvature $k(\lambda)$ reaches its maximum (**Equation [V]**):

$$k(\lambda) = \frac{\left| \rho'(\lambda)\eta''(\lambda) - \rho''(\lambda)\eta'(\lambda) \right|}{\left[\rho'(\lambda)^2 + \eta'(\lambda)^2 \right]^{\frac{3}{2}}} \quad \text{(V)}$$

Where $\rho(\lambda)=\log(\|d_{obs}\text{-}d_{cal}(m)\|)$, $\eta(\lambda)=\log(\|L(m\text{-}m_0)\|)$, and primes denote derivatives with respect to λ.

In implementation, 50 logarithmically spaced damping factors ranging from 10^{-3} to 10^{2} were tested based on preliminary sensitivity analyses. For each candidate λ, non-linear inversion was performed using the Levenberg–Marquardt algorithm with convergence criteria of relative change $<10^{-4}$ or a maximum of 100 iterations. The curvature $k(\lambda)$ was computed numerically from the resulting L-curve,[33] and the value maximizing $k(\lambda)$ was identified as the optimal balance point. The selected λ was validated by checking the geological plausibility of the inverted velocity model.

Introducing a damping factor effectively balances data-fitting accuracy and model complexity, avoiding unreasonable fluctuations in the model, especially under complex site conditions with high data noise or lateral heterogeneity in the subsurface structure.[34] Its regularization effect is crucial for improving the reliability of inversion results.[35] This study utilized parameter sensitivity testing to determine reasonable damping factor values and verified their positive effect in goaf identification, significantly improving the identification resolution of low-velocity anomalies such as cavities and fracture zones.

3.3. Equipment parameters

The node-type seismometer used in this experiment was the ANT-1C from Earth Pulse Technology Co., Ltd.

Figure 4. Ant-1C single-component nodal seismometer

Table 3. ANT-1C single-component (5 Hz) nodal seismometer specifications

Parameter	Indicator (%)
Natural frequency	5±7.5
DC resistance	1850±5
Sensitivity	80±5
Damping	0.6±7.5
Distortion	≤0.1
Aliasing	≥170

Abbreviation: DC: Direct current.

(China) (Figure 4). This instrument is highly sensitive, has a wide dynamic range, and is well-suited for field use, making it ideal for long-term field observations. The device supports sampling intervals of 0.25/0.5/1.0/2.0/4.0 ms (1.0 ms, i.e., 1,000 sps, was used in this experiment), with a typical main frequency band of 1–100 Hz (the low frequency can be set to 1 Hz, and the upper high-frequency limit is limited by the sampling rate and anti-aliasing filter). The instantaneous dynamic range can reach 126.8 dB (@0 dB, 1 ms), and the total dynamic range can reach 150 dB. The equivalent input noise is 0.22 μV (12 dB gain, 2 ms). Internal storage is configurable from 8 GB to a maximum of 32 GB (this unit has 32 GB); time accuracy is ±10 μs, and the device includes a built-in global positioning system (BeiDou Navigation Satellite System, China National Space Administration, China) for timing and positioning. Detailed device parameters are provided in Table 3.

3.4. Technical optimization

To improve the quality of surface wave dispersion extraction and the resolution of shear wave velocity profiles, the layout and acquisition parameters were specifically optimized for this exploration.[36] A linear array configuration was adopted instead of the traditional equilateral triangular array structure. Linear arrays have been demonstrated to provide more efficient spatial sampling through $N(N\text{-}1)/2$ independent station pairs and better azimuthal coverage for directional ambient noise sources typical of urban heritage environments.[37] This geometry is particularly advantageous in spatially constrained sites where elongated deployment corridors (e.g., roadsides and pathways) are

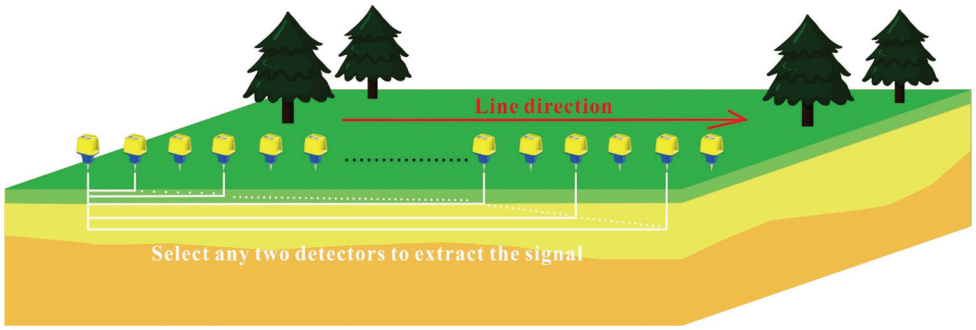

Figure 5. Extraction pattern diagram

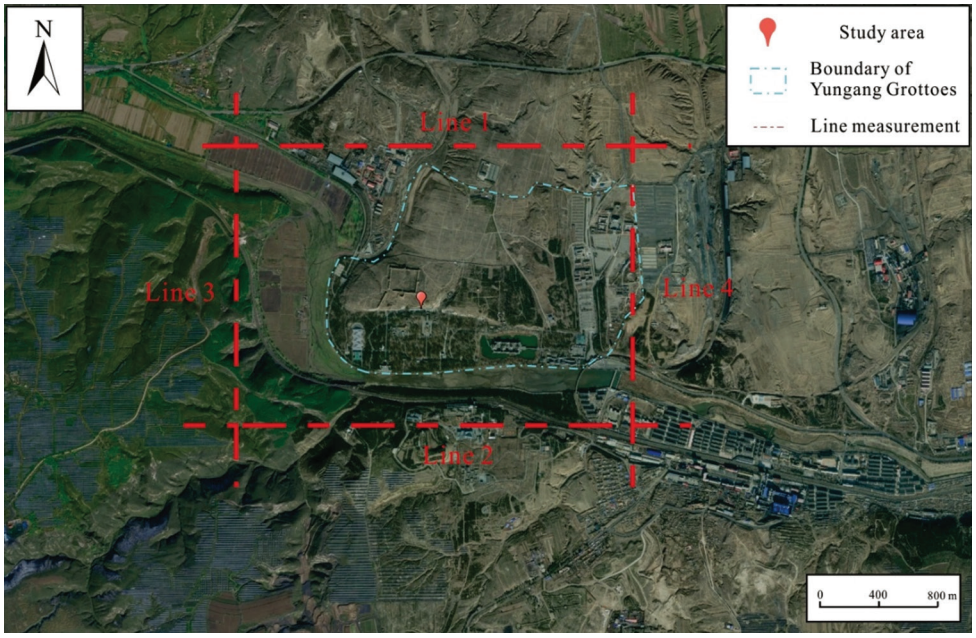

Figure 6. Schematic diagram of survey line arrangement

Table 4. Comparison with recent studies

Study	Array type	Damping strategy	Max depth (m)	Lateral res. (m)	RMS reduction	Application
This work	Linear, all-pairs	L-curve (0.20–0.35)	320	10–20	27%	Goafs, heritage
Ling *et al.*[9]	Circular	Fixed (0.15)	200	30–40	Not reported	Coal goafs
Li *et al.*[13]	2D grid	Tikhonov (0.20)	150	25–35	Not quantified	Fault imaging
Wang *et al.*[38]	Linear	None	180	40–50	N/A	Mine tunnels

Abbreviation: N/A: Not available; res.: Resolution; RMS: Root mean square.

Table 5. Statistics on surface wave exploration workload

Line arrangement	Length (m)	Coordinate points	Physical points
Line 1 (N)	3210	322	322
Line 2 (S)	3210	322	322
Line 3 (W)	2580	259	259
Line 4 (E)	2580	259	259

Abbreviations: E: East; N: North; S: South; W: West.

the only accessible options, as encountered in the Yungang Grottoes protection area.[38,39]

By adopting a processing method that extracts surface wave signals between any two stations (Figure 5), data information was fully utilized to achieve the highest possible spatial resolution in the imaging results. This combination of optimized array geometry and advanced signal processing effectively addresses the dual challenges of high-resolution subsurface imaging and non-invasive detection in sensitive cultural heritage environments.

3.5. Methodological innovations and performance metrics

This study introduced three key innovations that enhance imaging accuracy compared with conventional SPAC applications:

(i) Linear array with multi-pair processing: High-density linear arrays exploit $N(N\text{-}1)/2$ station pairs, yielding over 31,000 correlation pairs per survey line versus ~250 in conventional radial geometries.

(ii) L-curve-guided damping selection: Systematic curvature analysis across 50 candidates (10^{-3}–10^{2}) objectively determines λ_{opt}, eliminating subjective parameter selection.

(iii) Velocity-gradient-adaptive regularization: Optimized damping suppresses non-geological oscillations at sharp velocity contrasts (Δv_s>800 m/s).

The following quantitative improvements were observed compared with conventional fixed-λ inversion: (i) root mean square residual reduction: average 27% (8 Hz: 42.3→29.6 m/s); (ii) oscillation suppression: 58% reduction in velocity coefficient of variation (0.34→0.14); (iii) anomaly contrast enhancement: 1.6:1→2.1:1; and (iv) resolution gain: 15 m @ 100 m depth versus 25 m. Table 4 demonstrates the improved performance of the approach in this study compared with recent studies in maximum detection depth (320 m), lateral resolution (10–20 m), and RMS reduction (27%).

4. Experimental design and data processing

4.1. Measurement network layout

To obtain information on the shallow stratum shear wave velocity structure of the study area, four passive source surface wave lines, totaling 11.58 km in length, were laid out in the region, taking into account surface conditions and the distribution of underground safety red lines. A total of 1126 physical observation points were established, as depicted in Figure 6. The layout of the survey lines fully accounted for the distribution of goafs, surface accessibility, and acoustic signal coverage requirements. The overall layout was distributed in a north–south direction, following known underground safety control lines. The data are summarized in Table 5.

The spacing between each measurement point was moderate, with an average platform spacing of <10 m to ensure Rayleigh wave wavelength resolution while maintaining imaging accuracy. The on-site deployment employed a node-based cable-free connection, facilitating high-density deployment in densely built-up urban areas, along roadsides, or within cultural heritage protection zones, thereby effectively improving data integrity and spatial resolution.

4.2. Quality control

To ensure measurement accuracy and data quality, this experiment utilized a high-precision real-time kinematic-global navigation satellite system for real-time three-dimensional (3D) positioning of all node layout points. The horizontal positioning accuracy of the nodes was better than ±2 cm, and vertical elevation control accuracy was better than ±5 cm, meeting the strict requirements for station positioning in high-precision surface wave data inversion.

During data collection, a pass-rate verification mechanism and a real-time on-site monitoring system conducted multiple rounds of quality screening on the observed data. The physical point data in this study achieved a 100% pass rate. A total of 57 checkpoints were set up,

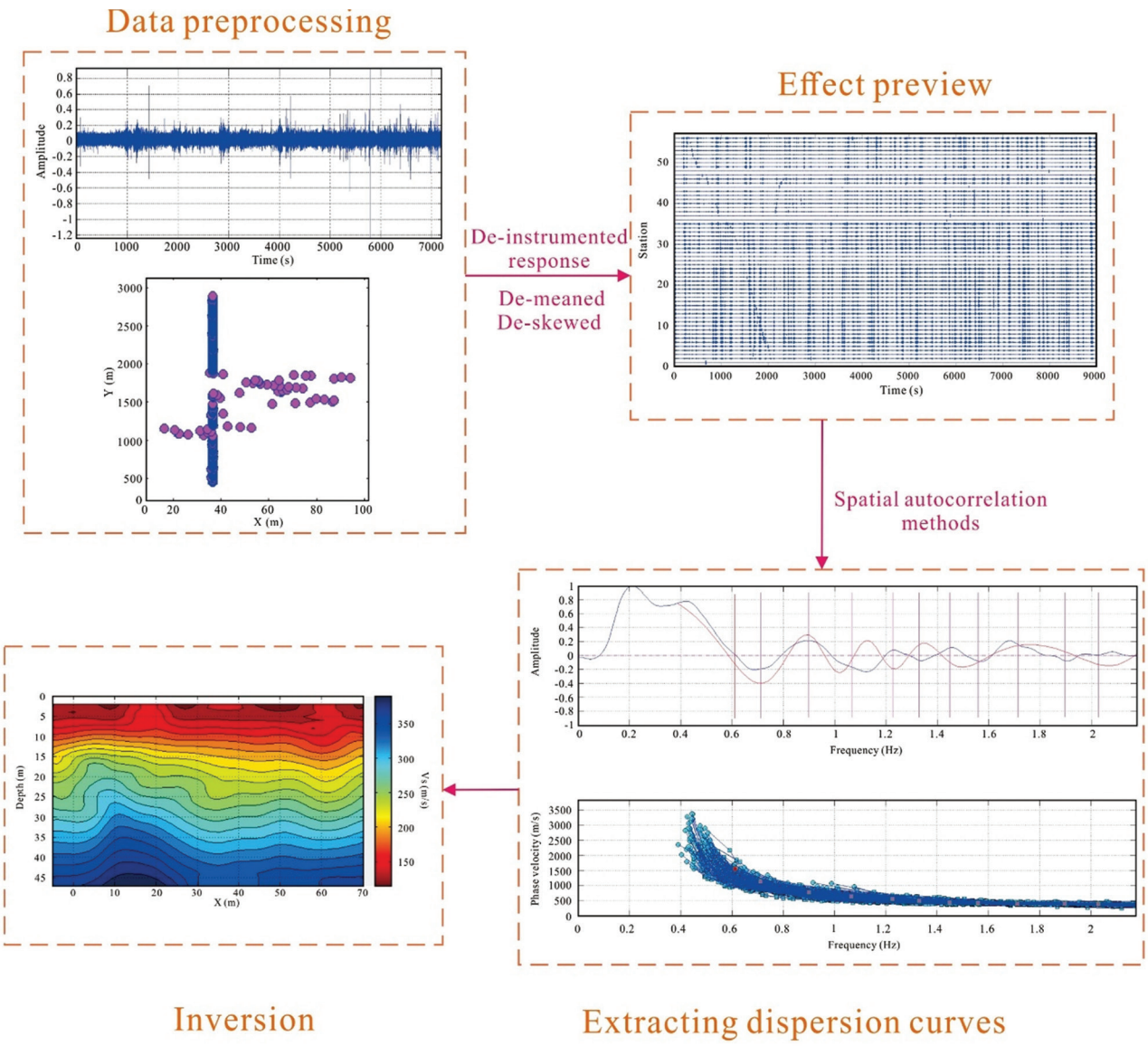

Figure 7. Flow chart of data processing

accounting for 5.02% of all measurement points, and each successfully passed full-waveform playback and spectrum analysis tests. No missed samples, incorrect recordings, or significant noise interference were detected, ensuring the authenticity and integrity of the data. Quantitative quality metrics show signal-to-noise ratio ranging from 15 to 45 dB across frequency bands of 2–15 Hz, with an average waveform correlation coefficient >0.85 between adjacent stations, confirming data reliability for dispersion analysis.

4.3. Data processing flow

After data acquisition, the microtremor data were processed and inverted using tomography. The specific process includes four stages: data preprocessing, dispersion analysis, velocity inversion, and anomaly interpretation. During processing, the original microtremor waveform was first subjected to noise filtering and waveform shaping, followed by the extraction of the dominant Rayleigh wave component to construct a frequency-phase velocity spectrum.[40] The dispersion curve extraction used multi-channel spectrum superposition technology to effectively suppress noise interference. The transverse wave velocity profile inversion utilized a multi-frequency co-inversion algorithm, supplemented by tomography technology to construct a 2D wave velocity structure, as shown in Figure 7.The specific method and process are as follows: using continuous waveform data recorded by the array, the

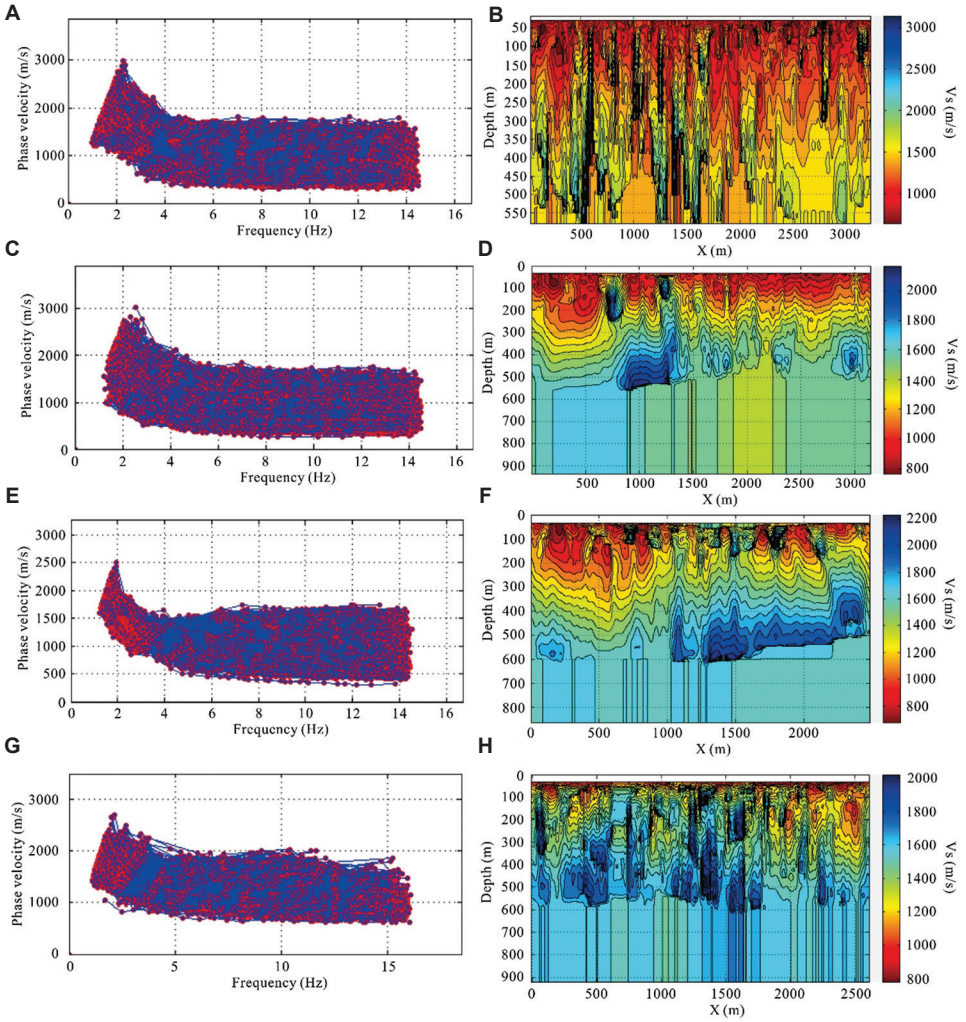

Figure 8. Dispersion curves and shear wave velocity profiles. (A) and (B) show the dispersion curves and two-dimensional velocity profiles for Line 1; (C) and (D) for Line 2; (E) and (F) for Line 3; and (G) and (H) for Line 4.

frequency domain waveform SPAC method was applied to obtain the surface wave Green's function between stations. The processing techniques include raw data preprocessing, such as instrument response removal, mean removal, tilt removal, and segmentation into unit-length data (e.g., minutes). Seismic signal interference was suppressed through preprocessing methods like sliding absolute value averaging. The processed waveforms were then spectrally whitened within the required frequency band. Next, the SPAC function between two stations was calculated every 2 min. Finally, the long-term autocorrelation function was superimposed as required, allowing further extraction of the surface wave dispersion curve.[41] For extracting surface wave dispersion curves, the SPAC method was used to derive surface wave phase velocity dispersion curves, while surface wave tomography obtained dispersion curves for each point beneath the array. Specifically, the inversion region was first divided into a grid, and the phase velocity distribution for each cycle is inverted to ultimately obtain a surface wave apparent velocity structure model of the medium beneath the array.[42]

4.4. Data imaging results

The survey consisted of four measurement lines, each comprising multiple seismic arrays and nodes strategically deployed to capture detailed subsurface shear wave velocity information. The specifics of each line's layout and data acquisition are as follows:

(i) Line 1 consists of two observation arrays. Array 1 was completed by 239 seismic stations at points 1083–1322, while Array 2 was completed using 246 seismic stations at points 1001–1246.

(ii) Line 2 also comprises two observation arrays. Array 1 includes 246 seismic stations at points 2001–2246,

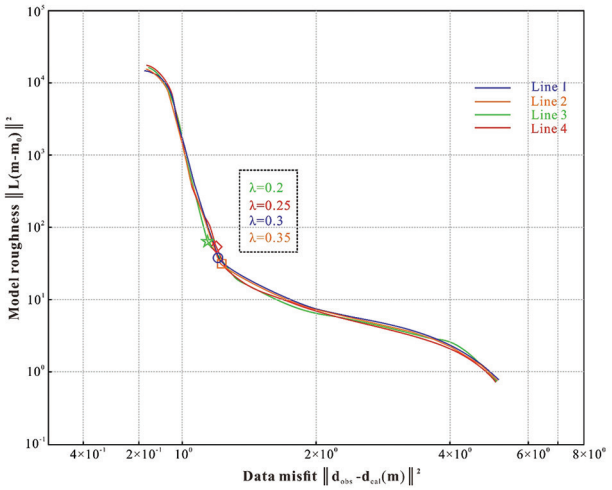

Figure 9. L-curve analysis for determining the optimal damping factors of the four survey lines. Notes: This figure presents the L-curve analysis used to select the optimal damping factors for the four survey lines. The horizontal axis represents the model norm ($\|d_{obs}\text{-}d_{cal}(m)\|$), while the vertical axis represents the residual norm ($\|L(m\text{-}m_0)\|$). Each curve shows the trade-off between model complexity and data fit at different damping factor values. The inflection point of each L-curve corresponds to the optimal damping factor, which balances model complexity and data misfit. The selected damping factors, located near the inflection points, ensure the stability and physical reasonableness of the inversion results.

and Array 2 includes 236 seismic stations at points 2076–2312.

(iii) Line 3 was completed with 246 nodes positioned between observation points 3008 and 3254, along with one seismograph.

(iv) Line 4 involved a total of 244 nodes from measurement points 4001 to 4259, observed by one seismograph, completing one observation.

The complete imaging results of these four lines are illustrated in Figure 8.

To determine the optimal damping factor for the regularized inversion, this study employed the L-curve criterion to quantitatively analyze the inversion results of four survey lines (Figure 9). The L-curve is a plot in double logarithmic coordinates, with the model norm ($\|d_{obs}\text{-}d_{cal}(m)\|$) on the horizontal axis and the residual norm ($\|L(m\text{-}m_0)\|$) on the vertical axis, generated by inverting a series of damping factors λ.[43] This curve reflects the trade-off between model complexity and data fitting accuracy: smaller λ values yield better data fitting but can produce overly complex models that amplify noise, whereas larger λ values enhance model stability at the cost of reduced spatial resolution and excessive smoothing. The inflection point of the curve is considered the parameter that provides the best compromise between noise suppression and model resolution, that is, the optimal balance between the two.[44]

As shown in Figure 9, the L-curves of all four measurement lines exhibit the characteristic "L" shape with clearly identifiable inflection points. The damping factors selected based on this criterion are all near the inflection points, indicating a successful balance between stability of the results and physical plausibility during inversion. This approach reduces subjective bias in parameter selection and provides quantitative evidence for the reliability of subsequent inversion results.

The final damping factors ranged between 0.20 and 0.35. By adjusting the damping parameters within this range, the inversion model effectively balanced fitting accuracy with stability, thereby improving the reliability of identifying low-velocity anomalous zones. Figure 10 compares the imaging results before and after damping factor adjustment, showing that detection depth covers a range from 50 to 320 m, with lateral resolutions of approximately 10–20 m. The effects of seismic station distribution and terrain undulations are also well captured in the imaging.

4.5. Resolution verification

Synthetic checkerboard tests (Δv_s= ±20%, 15 m × 20 m spacing) validated the stated resolution using Table 2 velocities and λ=0.25. The results were as follows: (i) 15 m features were resolved at depth <150 m (correlation >0.75); (ii) 20 m features were resolved at 150–250 m (correlation >0.70); and (iii) detectability extended to 320 m for ±15% contrasts.

A synthetic goaf (40 m wide, 8 m thick, v_s=1,000 m/s at 120 m) was recovered with <5 m horizontal and <3 m vertical errors, validating the observed goaf dimensions (50–200 m extent, 2–10 m thickness).

5. Results analysis and validation

5.1. Goaf identification mark

Low-velocity anomalies were identified through shear wave velocity inversion profiles, providing an effective physical parameter basis for goaf identification.[45,46] Research demonstrates that goafs exhibit significantly low-velocity characteristics in wave velocity imaging, with shear wave velocities generally below 1,200 m/s, clear boundary contours, and mostly band-shaped or lens-shaped anomalies. This velocity threshold, combined with on-site lithology, engineering history, and mine area data analysis, is used as the main geophysical indicator for determining the existence of goafs.[47-49]

Multi-level goafs often manifest as sudden drops in vertical velocity accompanied by increased velocity fluctuations, while horizontally they appear as continuous

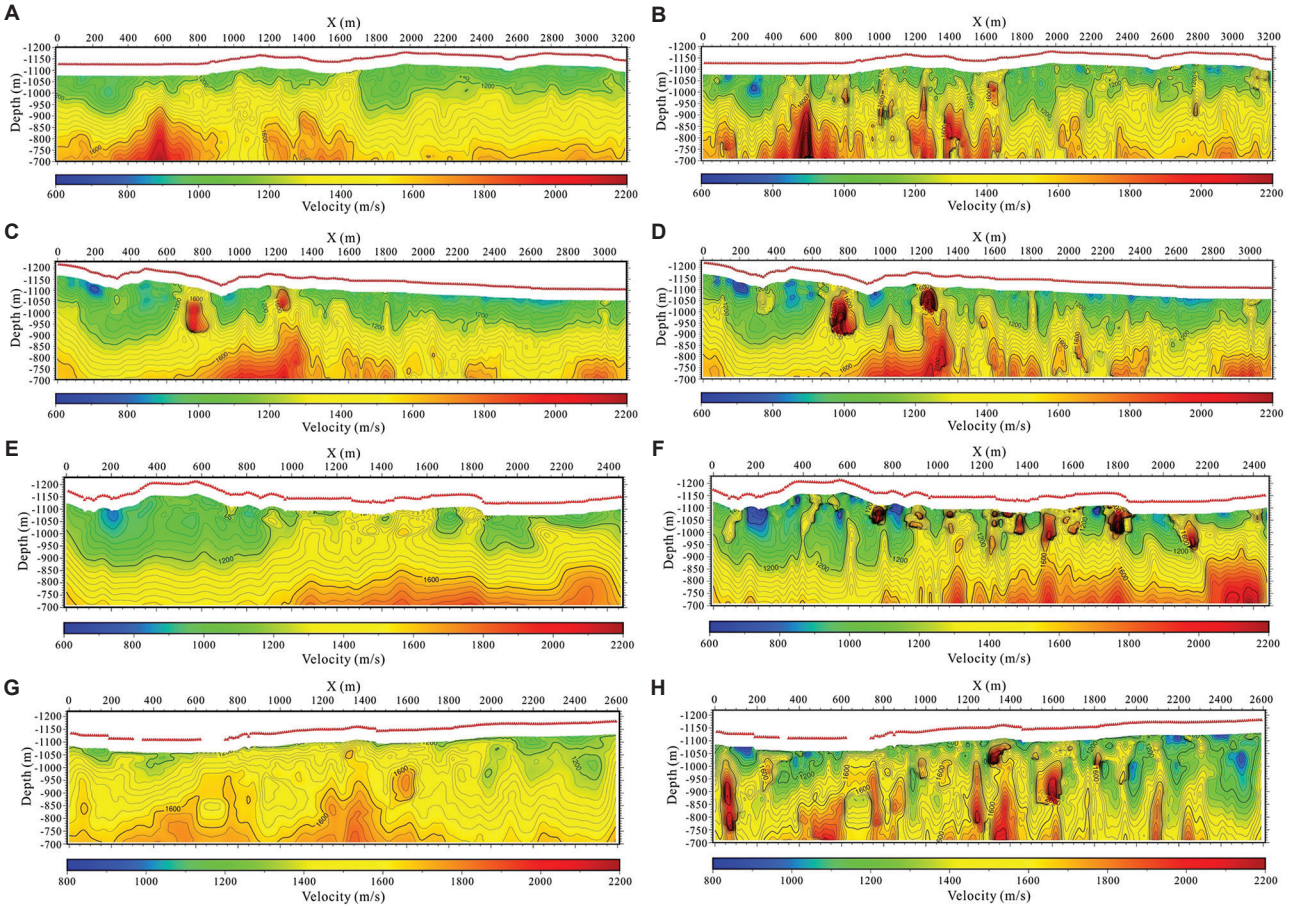

Figure 10. Comparison before and after adjustment of the damping factor. (A) Line 1, unadjusted damping factor. (B) Line 1, adjusted damping factor. (C) Line 2, unadjusted damping factor. (D) Line 2, adjusted damping factor. (E) Line 3, unadjusted damping factor. (F) Line 3, adjusted damping factor. (G) Line 4, unadjusted damping factor. (H) Line 4, adjusted damping factor.

low-velocity zones with wave velocity gradients significantly weaker than those of the surrounding normal rock. These characteristics provide parameter support for subsequent anomaly boundary delineation and stratification analysis.

5.2. Distribution pattern analysis

In this study, through systematic analysis of the wave impedance tomography results from four survey lines (L1 – N line, L2 – S line, L3 – W line, and L4 – E line), multiple typical low-velocity anomaly zones were identified. Combined with historical mining data, borehole records, and topographical information, their causes were accurately determined, as shown in Figure 11. The distribution of these anomalies is highly correlated with historical mining activities in the region, mainly manifested in a significant decrease in the apparent wave velocity at the depth of the coal seam and a concave wave velocity contour line, which are typical geophysical response characteristics of goafs.

Line 1 runs along the north side of the Yungang Grottoes and crosses several historical mining areas. The imaging results showed multiple coal seams with overlapping goafs along this line. Among them, the area between pile numbers 400–440 m (Line 1-1) is located beneath the riverbed of the Shilihe River, where wave velocity anomalies were significant. Based on historical data, this anomaly is inferred to be caused by the mining of coal seams #2, #3, and #7. The section between pile numbers 610 and 1,530 m (Line 1-2 to Line 1-4) also demonstrated pronounced low-velocity anomalies, which coincide with the mining activities of coal seams #2 and #3 at the Wuguantun Mine. The section between pile numbers 1,700 and 2,000 m (Line 1-5) is an area where multiple coal seams were jointly mined in the history of the Wuguantun Mine. The mining seams include #2, #7, #11-3, and #12. In the 2,140–2,930 m section (Line 1-6), low velocity anomalies extend deeply into coal seams #2, #3, and #7, reflecting multi-level mining characteristics.

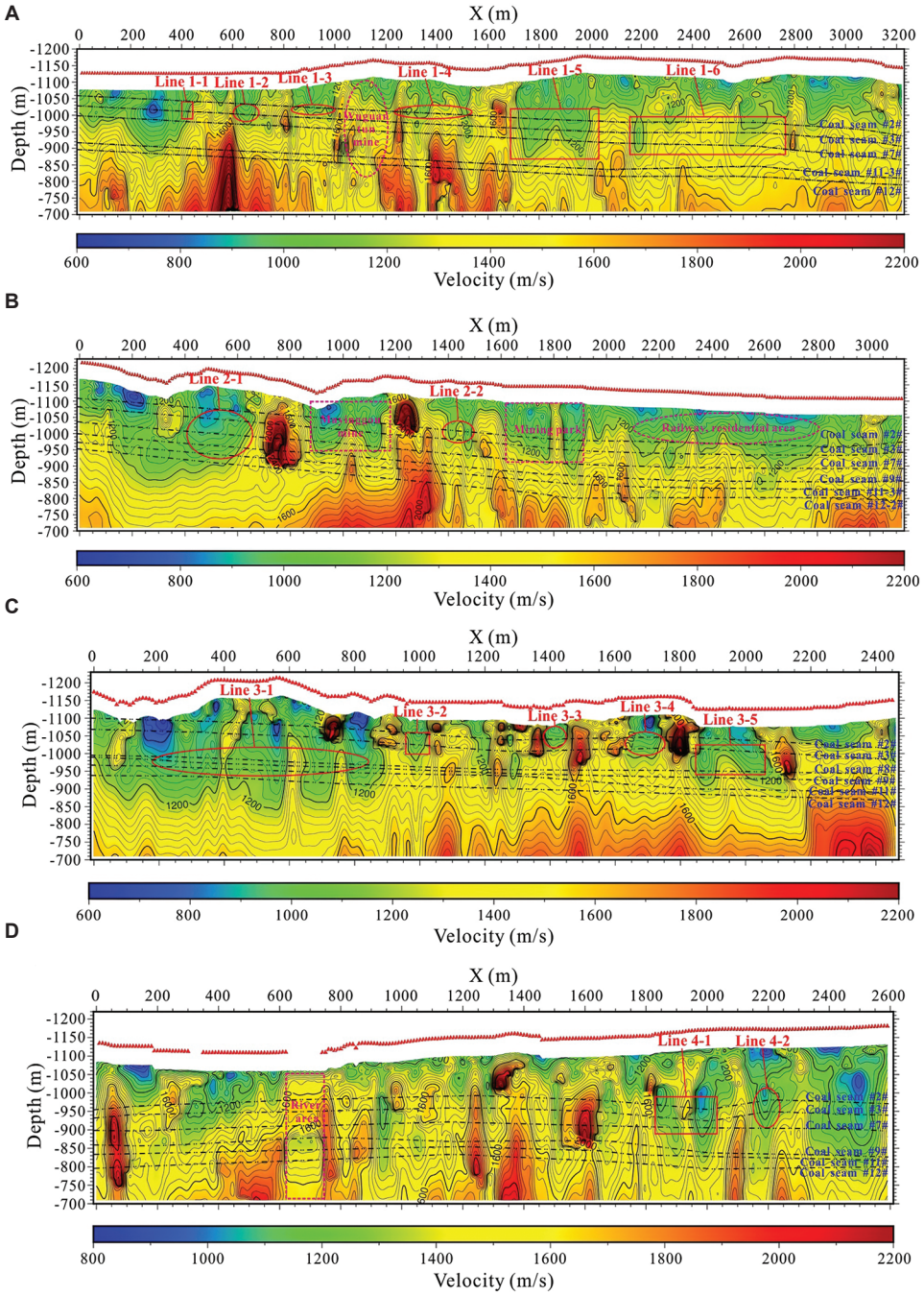

Figure 11. Transverse wave velocity profile interpretation diagram. (A) Line 1 two-dimensional (2D) velocity profile interpretation. (B) Line 2 2D velocity profile interpretation. (C) Line 3 2D velocity profile interpretation. (D) Line 4 2D velocity profile interpretation.

Line 2 is located on the south side of the Yungang Grottoes. The layer imaging results showed that multiple coal seams simultaneously exhibit significant reductions in wave velocity in the vertical direction, which is a typical feature of multi-layer mining. The section between pile numbers 400 and 660 m (Line 2-1) is a historically known goaf area of coal seams #9 and #12. The imaging results also indicate that the lower coal seams #2 and #3 experience a decrease in wave velocity and contour line disturbances. Combined with drilling data and mining records, this is inferred to be a multi-level superimposed goaf area. In addition, an isolated low-velocity anomaly occurs in the section between pile numbers 1,370 and 1,500 m (Line 2-2), for which no clear mining records exist. It is

speculated that this anomaly results from a hidden void structure caused by small-scale mining.

Line 3 runs along the west side of the Yungang Grottoes. Within the range of pile numbers 320–920 m (Line 3-1), the results correspond to the mining records of coal seams #7–3, #9, and #12. The tomography depicts consistently low wave velocity and continuous structure, confirming the impact of multiple-seam mining. At 950–1,020 m (Line 3-2), a small kiln mining zone exhibits obvious wave velocity anomalies. In addition, three low-velocity anomaly zones (Line 3-3 to Line 3-5) are distributed in the Shilihe riverbed section (pile numbers 1380–2060 m), characterized by significant wave velocity concavity and the development of a fracture zone in the deeper parts of coal seams #2 and #3.

Line 4 is laid out on the east side of the Yungang Grottoes. The imaging results revealed two significant low-velocity anomaly zones distributed between pile numbers 1,830 and 2,250 m. In Line 4-1 (1,830–2,030 m), the regional wave impedance image shows low-velocity anomalies in the deeper coal seams, which are presumed to be goafs formed by the joint mining of coal seams #2 and #3 in small kilns. In the Line 4-2 section (2,160–2,250 m), the wave velocity ranges between 1,000 and 1,200 m/s, typical of the #7-1 coal seam mining reflection characteristics. At the same time, the #2 and #3 coal seams also display abnormal responses, indicating the existence of multiple layers of superimposed mining.

5.3. Summary of achievements

Through systematic and standardized field geophysical exploration, data processing, and comprehensive interpretation, combined with the results of field investigations, the distribution range of the main coal seam goafs below the geophysical survey lines in the protected area has been basically identified. When analyzing the extent of the goafs, mining data collected from the three coal mines surrounding the Yungang Grottoes were fully integrated. Finally, through comparative analysis and integration with known hydrogeological data, the extent of the goafs of each coal seam along the underground safety line of the Yungang Grottoes was delineated.

The extent of the goafs delineated along each survey line is described below:

(i) L1 survey line
Line 1-1 is inferred to represent small kiln mining voids in coal seams #2 and #3, with a 300 m range located outside the boundary and a 40 m range located on the Yungang Grottoes underground safety line. Line 1-2 is presumed to represent small mine workings in coal seams #2 and #3, with an area of 80 m. Line 1-3 is also presumed to represent small mine workings in coal seams #2 and #3, with an area of 170 m. Line 1-4 is inferred to be a small kiln mining void in coal seams #2 and #3, with a range of 260 m. Line 1-5 is inferred to be a multi-layer goaf of coal seams #2, #3, #7, and #11, with a range of 340 m. Line 1-6 is presumed to be a multi-layer goaf of coal seams #2, #3, and #7-3, with a range of 870 m, of which 170 m lies outside the boundary.

(ii) L2 survey line
Line 2-1 is inferred to represent multiple goafs of coal seams #2, #3, #7-1, #9, and #12, with a total goaf range of 670 m, of which 270 m lies on the underground safety line of the Yungang Grottoes, corresponding to the goaf of coal seam #9. The 400 m range located outside the boundary includes the 0–210 m section corresponding to the goaf of the #7-1 coal seam working face, and the 210–400 m section corresponding to the multi-layer goaf of the #7-1, #9, and #12 coal seams. Line 2-2 is presumed to represent small kiln mining voids in coal seams #2 and #3, with a range of 800 m, of which 620 m corresponds to the current surface of the mining park.

(iii) L3 survey line
Line 3-1 represents a comprehensive inference of multiple goafs in coal seams #2, #3, #7-1, #9, and #12, with a total range of 980 m, of which 580 m lies on the underground safety line of the Yungang Grottoes. The 400–520 m section corresponds to the multi-layer goaf of coal seams #7-1, #9, and #12, the 520–910 m section corresponds to the multi-layer goaf of coal seams #7-1 and #9, and the 910–980 m section corresponds to the goaf of coal seam #7-1. Line 3-2 is inferred to be a multi-layer goaf of coal seams #2, #3, and #7-1, with a range of 80 m. Line 3-3 is presumed to be the goaf of coal seams #2 and #3, with a range of 80 m. Line 3-4 is presumed to be the goaf of small kilns in coal seams #2 and #3, with a range of 127 m. Line 3-5 is presumed to be the goaf of small kilns in coal seams #2 and #3, with a range of 220 m.

(iv) L4 survey line
Line 4-1 is inferred to be a small kiln goaf in coal seams #2 and #3, with a range of 225 m. Line 4-2 is inferred to be a multi-layer goaf in coal seams #2, #3, and #7, with a range of 300 m, of which 70 m lies on the underground safety line of the Yungang Grottoes.

A total of 15 anomalous goafs were identified, including eight historical goafs from small coal mines. The anomalies are widely distributed along the L1 to L4 survey lines, showing a multi-center distribution pattern with densely developed goafs in local sections. This reflects the multi-level superimposed effects formed by coal mining activities during different historical periods. Lines 1 and 4 exhibit a high concentration of mining anomalies, characterized by

large areas of low wave velocity, significant depth extension, and complex structural characteristics.

The goafs of small local coal mines are scattered and isolated, mostly concentrated near the intersection of survey lines and areas with uneven terrain, which may be related to early manual mining methods and terrain control. Although such small goafs are small in volume, they have a significant impact on geological structural integrity and engineering safety.

5.4. Implications for grotto stability

The identified low-velocity anomalies present varying geological risks depending on their spatial distribution, depth, and velocity characteristics. Four anomalies within the safety boundary (Line 1-1: 40 m, Line 2-1: 270 m, Line 3-1: 580 m, and Line 4-2: 70 m), located at depths of 50–180 m, pose potential subsidence risks.[50] Multi-layer goafs, such as L2-1, significantly increase the likelihood of progressive failure and accelerate weathering processes.

A shear wave velocity (v_s) below 1,200 m/s indicates highly fractured rock compared with intact rock (v_s>2,000 m/s). Using the empirical relationship rock quality designation (RQD)≈$0.01\times v_s^{1.35}$, a velocity of 1,200 m/s yields an RQD of approximately 28%, classifying the rock mass as "very poor" with low load-bearing capacity.[51]

The distribution of goafs also leads to stress concentrations 2–3 times higher than the lithostatic pressure,[52] increasing the risks of progressive roof collapse, surface fissuring in shallow goaf areas (<100 m depth), and asymmetric loading on structural pillars. Areas with water accumulation, such as Line 3-3 to Line 3-5, exhibit v_s<1,000 m/s, suggesting weakened rock strength, increased weathering, and susceptibility to freeze–thaw damage.

Risk zoning can be categorized as follows: (i) high-risk zones, within 50 m of the safety boundary, with v_s<1000 m/s and multi-layer goafs, require immediate monitoring and possible grouting; (ii) moderate-risk zones, between 50–150 m with v_s between 1,000–1,200 m/s, should undergo periodic surveys; and (iii) low-risk zones, beyond 200 m with isolated small goafs, should be monitored over the long-term.

Recommended monitoring techniques include global navigation satellite system surface deformation measurements, repeat SPAC surveys every 2–3 years, groundwater level monitoring, and InSAR for regional subsidence detection.[53]

5.5. Methodological transferability and limitations

The SPAC method is highly transferable to cultural heritage sites facing subsurface hazards, such as mining-affected monuments (e.g., Longmen and Mogao), karst sites,[54,55] and urban heritage zones with voids. Its non-invasive, ambient-noise-based operation aligns with conservation protocols, making it suitable for sensitive environments where traditional geophysical methods are restricted.

Key prerequisites include sufficient ambient noise, station spacing ≤0.3 × depth, and favorable geological conditions (avoiding high water tables >5 m). For shallow depths (<100 m), 5 Hz sensors are sufficient, while broadband sensors are required for deeper targets (>200 m). The optimal damping factor (λ=0.20–0.35), selected using L-curve analysis, is suitable for moderate velocity contrasts.

Limitations include electromagnetic interference (1–5 Hz), ambiguity in distinguishing natural and anthropogenic voids (both exhibiting v_s<1,200 m/s), and depth trade-offs (small voids <5 m at depths >150 m may require ground-penetrating radar or microgravity surveys).

Verification can be achieved through drilling (Line 1-1, Line 2-1, Line 3-1, and Line 4-2), ERT for water-filled voids (<50 Ω·m), microgravity surveys with 5 m spacing, repeat SPAC/InSAR (Δv_s<−5%), and 3D modeling for engineering-grade characterization.

6. Conclusion

Based on the urgent need for detailed detection of underground goafs in the Yungang Grottoes Protection Area, this study introduced the SPAC method combined with damping-optimized inversion to carry out systematic geophysical detection. The following main conclusions were reached:

(i) High-density linear arrays achieved 10–20 m lateral resolution and a maximum depth of 320 m, overcoming traditional imaging limitations in spatially constrained heritage sites.
(ii) Damping regularization (λ = 0.20–0.35) effectively suppresses velocity oscillations at sharp contrasts, improving model stability and goaf identification accuracy.
(iii) Fifteen low-velocity anomalies (v_s<1200 m/s) were identified, corresponding to historical mining of coal seams 2#, 3#, 7#, 9#, and 12#. Critical anomalies beneath the grotto core area pose significant geological hazard risks.
(iv) The non-invasive SPAC method achieves high-precision imaging without surface disturbance or artificial sources, demonstrating strong engineering adaptability for cultural heritage protection.
(v) The results provide a scientific basis for stability assessment and risk management, supporting heritage

protection planning, goaf treatment, and safety supervision.

(vi) The framework is applicable to mining temples, karst sites, urban zones with sufficient noise, station spacing ≤0.3 × depth, and favorable geological conditions. L-curve damping (0.1–0.5) is universally applicable, while site-specific calibration optimizes performance.

(vii) Limitations include inversion non-uniqueness; ambiguity in interpreting v_s<1,200 m/s (needing borehole or ERT verification), near-surface bias (<30 m), and resolution degradation >200 m. The damping assumption of smoothness; abrupt contrasts need tuning. Multi-method integration is essential.

Overall, SPAC-damping optimization effectively achieves 10–20 m horizontal resolution and 320 m depth imaging without excavation and is transferable to World Heritage Sites for evidence-based risk management.

Acknowledgments

None.

Funding

This research was funded by the National Key Research and Development Project (grant number 2022YFC2903402).

Conflict of interest

The authors declare that they have no competing interests.

Author contributions

Conceptualization: Jiale Liu, Xiaodong Wang
Formal analysis: Jiale Liu, Xiaodong Wang
Investigation: Jiale Liu, Yanhai Liu, Ke Ren, Shangqing Zhang
Methodology: Jiale Liu, Xiaodong Wang
Visualization: Jiale Liu
Writing–original draft: Jiale Liu
Writing–review and editing: Jiale Liu, Xiaodong Wang, Yanhai Liu, Ke Ren

Availability of data

Due to confidentiality constraints, the data analyzed in this study are not available for public dissemination.

References

1. Vadrucci M. Sustainable cultural heritage conservation: A challenge and an opportunity for the future. *Sustainability*. 2025;17(2):584.

   doi: 10.3390/su17020584

2. Huang J, Ren J. Geophysical prospecting method applied in the preservation of Yungang Grottoes. *Sci Conserv Archaeol*. 2011;23(2):87-95.

   doi: 10.16334/j.cnki.cn31-1652/k.2011.02.007

3. Galdón JM, Rey J, Martínez J, Hidalgo MC. Application of geophysical prospecting techniques to evaluate geological-mining heritage: The Sinapismo mine (La Carolina, Southern Spain). *Eng Geol*. 2017;138:71-78.

   doi: 10.1016/j.enggeo.2017.01.012

4. Martinho E, Dionísio A. Main geophysical techniques used for non-destructive evaluation in cultural built heritage: A review. *J Geophys Eng*. 2014;11(5):053001.

   doi: 10.1088/1742-2132/11/5/053001

5. Alao JO, Lawal KM, Dewu BBM, Raimi J. Construction of a multi-purpose geophysical test site on a lateritic clay soil. *Arab J Geosci*. 2024;17:238.

   doi: 10.1007/s12517-024-12039-72

6. Alao JO, Lawal KM, Dewu BBM, Raimi J. Near-surface seismic refraction anomalies due to underground target models and their application in civil and environmental engineering. *Phys Chem Earth Parts A/B/C*. 2025;138:103845.

   doi: 10.1016/j.pce.2024.103845

7. Perski Z, Hanssen R, Wojcik A, Wojciechowski T. InSAR analyses of terrain deformation near the Wieliczka Salt Mine, Poland. *Eng Geol*. 2009;106(1-2):58-67.

   doi: 10.1016/j.enggeo.2009.02.014

8. Xu PF, Li CJ, Ling SQ, Zhang YB, Hou Z, Sun YJ. Mapping collapsed columns in coal mines utilizing Microtremor Survey Methods. *Chin J Geophys*. 2009;52(7):1923-1930.

   doi: 10.3969/j.issn.0001-5733.2009.07.028

9. Ling S, Ren Q, Cheng F, *et al*. Application of microtremor survey technology in a coal mine goaf. *Appl Sci*. 2023;13(1):466.

   doi: 10.3390/app13010466

10. Martínez-Moreno FJ, Pedrera A, Ruano P, *et al*. Combined microgravity, electrical resistivity tomography, and induced polarization to detect deeply buried caves: Algaidilla cave (Southern Spain). *Eng Geol*. 2013;162:67-78.

    doi: 10.1016/j.enggeo.2013.05.008

11. Metwaly M, AlFouzan F. Application of 2-D geoelectrical resistivity tomography for subsurface cavity detection in the eastern part of Saudi Arabia. *Geosci Front*. 2013;4(4):469-476.

    doi: 10.1016/j.gsf.2012.12.005

12. Styles P, McGrath R, Thomas E, Cassidy NJ. The use of microgravimetry for cavity characterization in karstic terrains. *Q J Eng Geol Hydrogeol*. 2005;38(2):155-169.

    doi: 10.1144/1470-9236/04-035

13. Li Q, Zhang H, Lei X, Li C. Imaging of upper breakpoints of buried active faults through microtremor survey technology. *Earth Planets Space*. 2024;76:132.

    doi: 10.1186/s40623-024-02080-x

14. Liu Y, Xia J, Guan B, Xi C, Ning L, Zhang H. Short-term synchronous and asynchronous ambient noise tomography in urban areas: Application to karst investigation. *Engineering*, 2025;48:292-308.

doi: 10.1016/j.eng.2025.02.001

15. Alao JO, Lawal KM, Dewu BBM, Raimi J. Detection of shallow underground targets using electrical resistivity tomography and the implications in civil/environmental engineering. *Discov Geosci*. 2024;2:52.

doi: 10.1007/s44288-024-00058-6

16. Zeid AN, Corradini E, Bignardi S, Nizzo V, Santarato G. The passive seismic technique 'HVSR' as a reconnaissance tool for mapping paleo-soils: The case of the Pilastri archaeological site, Northern Italy. *Archaeol Prospect*. 2017;24(3):245-258.

doi: 10.1002/arp.1568

17. Schwellenbach I, Hinzen K, Petersen MG, Bottari C. Combined use of refraction seismic, MASW, and ambient noise array measurements to determine the near-surface velocity structure in the Selinunte Archaeological Park, SW Sicily. *J Seismol*. 2020;24:753-776.

doi: 10.1007/s10950-020-09909-4

18. Huang X, Guo F, Zhao L, Zhang F. Chemical weathering records in Yungang Formation, North China: Implications for stone heritage conservation. *Front Earth Sci*. 2025;13:1507580.

doi: 10.3389/feart.2025.1507580

19. Zhang Y, Shi W, Dong S, Wang T, Yang Q. Jurassic intracontinental deformation of the central North China Plate: Insights from syn-tectonic sedimentation, structural geology, and U-Pb geochronology of the Yungang Basin, North China. *Tectonophysics*. 2020;778:228371.

doi: 10.1016/j.tecto.2020.228371

20. Liu A, Xu Y, Liu C, Pang E. Geological characteristics and tectonic evolution of Datong Basin. *Geoscience*. 2021;35(5):1296-1310.

doi: 10.19657/j.geoscience.1000-8527.2020.067

21. Chen B, Yu X, Wang T, Ma F, Li S, Yang L. Lithofacies and architectural characteristics of sandy braided river deposits: A case from outcrops of the Middle Jurassic Yungang Formation in the Datong Basin, Shanxi Province. *Oil Gas Geol*. 2015;36(1):111-117.

doi: 10.11743/ogg20150114

22. Huang J. Study on the geological characteristics of the Yungang Grottoes. *Southeast Cult*. 2003;5:91-93.

23. Guo Y, Qin Y, Chen P, Xu N. Simulation of the compaction behavior and the water permeability evolution of broken rock masses of different shapes in a goaf. *Water*. 2023;15(6):1190.

doi: 10.3390/w15061190

24. Berryman JG. Seismic waves in rocks with fluids and fractures. *Geophys J Int*. 2007;171(2):954-974.

doi: 10.1111/j.1365-246X.2007.03563.x

25. Yang H, Duan HF, Zhu J, Zhao Q. Water effects on elastic S-wave propagation and attenuation across single clay-rich rock fractures: Insights from ultrasonic measurements. *Rock Mech Rock Eng*. 2024;57:2645-2659.

doi: 10.1007/s00603-023-03712-6

26. Aki K. Space and time spectra of stationary stochastic waves with special reference to microtremors. *Bull Earthq Res Inst Univ Tokyo*. 1957;35:415-456.

27. Xu P, Li S, Ling S, Guo H, Tian B. Application of SPAC method to estimate the crustal S-wave velocity structure. *Chin J Geophys*. 2013;56(11):3846-3854.

doi: 10.6038/cjg20131126

28. Xu P, Ling S, Li C, *et al*. Mapping deeply-buried geothermal faults using microtremor array analysis. *Geophys J Int*. 2012;188(1):115-122.

doi: 10.1111/j.1365-246X.2011.05266.x

29. Tarantola A, Valette B. Inverse problems = Quest for information. *J Geophys*. 1981;50(1):159-170.

30. Tikhonov AN. Solution of incorrectly formulated problems and the regularization method. *Sov Math Dokl*. 1963;5:103-114.

31. Phillips DL. A technique for the numerical solution of certain integral equations of the first kind. *J ACM*. 1962;9(1):84-97.

doi: 10.1145/321105.321114

32. Hansen PC, O'Leary DP. The use of the L-curve in the regularization of discrete ill-posed problems. *SIAM J Sci Comput*. 1993;14(6):1487-1503.

doi: 10.1137/0914086

33. Castellanos JL, Gómez S, Guerra V. The triangle method for finding the corner of the L-curve. *Appl Numer Math*. 2002;43(4):359-373.

doi: 10.1016/S0168-9274(01)00179-9

34. Haney MM, Tsai VC. Perturbational and nonperturbational inversion of Rayleigh-wave velocities. *Geophysics*. 2017;82(3):F15-F28.

doi: 10.1190/geo2016-0397.1

35. Ortega-Culaciati F, Simons M, Ruiz J, Rivera L, Díaz-Salazar N. An EPIC Tikhonov regularization: Application to quasi-static fault slip inversion. *J Geophys Res Solid Earth*. 2021;126(7):e2020JB021141.

doi: 10.1029/2020JB021141

36. Okada H. Theory of efficient array observations of microtremors with special reference to the SPAC method. *Explor Geophys*. 2006;37(1):73-85.

doi: 10.1071/EG06073

37. Cheng F, Xia J, Xu Y, Xu Z, Pan Y. A new passive seismic method based on seismic interferometry and multichannel analysis of surface waves. *J Appl Geophys*. 2015;117:126-135.

doi: 10.1016/j.jappgeo.2015.04.005

38. Wang K, Qian J, Zhang H, Gao J, Bi D, Gu N. Seismic imaging of mine tunnels by ambient noise along linear arrays. *J Appl Geophys*. 2022;203:104718.

doi: 10.1016/j.jappgeo.2022.104718

39. Langston CA. Spatial gradient analysis for linear seismic arrays. *Bull Seismol Soc Am*. 2007;97(1):265-280.

doi: 10.1785/0120060100

40. Hayashi K, Asten MW, Stephenson WJ, *et al*. Microtremor array method using spatial autocorrelation analysis of Rayleigh-wave data. *J Seismol*. 2022;26:601-627.

doi: 10.1007/s10950-021-10051-y

41. Nishida K, Takagi R, Takeo A. Ambient noise multimode surface wave tomography. *Prog Earth Planet Sci*. 2024;11:4.

doi: 10.1186/s40645-023-00605-8

42. Haney MM, Mikesell TD, van Wijk K, Nakahara H. Extension of the spatial autocorrelation (SPAC) method to mixed-component correlations of surface waves. *Geophys J Int*. 2012;191(1):189-206.

doi: 10.1111/j.1365-246X.2012.05597.x

43. Hansen PC. Analysis of discrete ill-posed problems by means of the L-curve. *SIAM Rev*. 1992;34(4):561-580.

doi: 10.1137/1034115

44. Yu D, Hwang C, Zhu H, Ge S. The Tikhonov-L-curve regularization method for determining the best geoid gradients from SWOT altimetry. *J Geod*. 2023;97:93.

doi: 10.1007/s00190-023-01783-5

45. Xia J, Miller RD, Park CB. Estimation of near-surface shear-wave velocity by inversion of Rayleigh waves. *Geophysics*. 1999;64(3):691-700.

doi: 10.1190/1.1444578

46. Mordret A, Landès M, Shapiro NM, Singh SC, Roux P. Ambient noise surface wave tomography to determine the shallow shear velocity structure at Valhall: Depth inversion with a Neighbourhood Algorithm. *Geophys J Int*. 2014;198(3):1514-1525.

doi: 10.1093/gji/ggu217

47. Cao B, Wang J, Du H, Tan Y, Liu G. Research on comprehensive detection and visualize of hidden cavity goaf. *Sci Rep*. 2022;12:22309.

doi: 10.1038/s41598-022-26680-3

48. Cao A, Dou L, Cai W, Gong S, Liu S, Jing G. Case study of seismic hazard assessment in underground coal mining using passive tomography. *Int J Rock Mech Min Sci*. 2015;78:1-9.

doi: 10.1016/j.ijrmms.2015.05.001

49. Zhou L, Jia B, Bao X, Chen H, Zheng K. Construction and experimental verification of wave velocity model for source location in goaf overlying rock strata. *J Appl Geophys*. 2024;230(2):105515.

doi: 10.1016/j.jappgeo.2024.105515

50. Arifuggaman A, Zhang C, Feng M, Chen Y, Li Q, Wang T. Mining-induced subsidence predicting and monitoring: A comprehensive review of methods and technologies. *Geotech Geol Eng*. 2025;43:314.

doi: 10.1007/s10706-025-03271-3

51. Barton N. Some new Q-value correlations to assist in site characterisation and tunnel design. *Int J Rock Mech Min Sci*. 2002;39(2):185-216.

doi: 10.1016/S1365-1609(02)00011-4

52. Ghabraie B, Ren G, Zhang X, Smith J. Physical modelling of subsidence from sequential extraction of partially overlapping longwall panels. *Int J Coal Geol*. 2015; 140:71-83.

doi: 10.1016/j.coal.2015.01.004

53. Bell FG, Stacey TR, Genske DD. Mining subsidence and its effect on the environment: Some differing examples. *Environ Geol*. 2000;40(1-2):135-152.

doi: 10.1007/s002540000140

54. Martínez-Pagán P, Navarro M, Pérez-Cuevas J, Alcalá FJ, García-Jerez A, Vidal F. Shear-wave velocity based seismic microzonation of Lorca city (SE Spain) from MASW analysis. *Near Surf Geophys*. 2014;12(6):412-423.

doi: 10.3997/1873-0604.2014032

55. Leucci G, De Giorgi L. Microgravimetric and ground penetrating radar geophysical methods to map the shallow karst network in a coastal area (Marina di Capilungo, Lecce - Italy). *Explor Geophys*. 2010;41(3):178-188.

doi: 10.1071/EG09029